ACS NANO
Cite This: ACS Nano XXXX, XXX, XXX–XXX
www.acsnano.org

ARTICLE

Quantifying the Ligand-Coated Nanoparticle Delivery to Cancer Cells in Solid Tumors

Qin Dai,[†] Stefan Wilhelm,[‡] Ding Ding,[§] Abdullah Muhammad Syed,[†] Shrey Sindhwani,[†] Yuwei Zhang,[∥] Yih Yang Chen,[†] Presley MacMillan,[∥] and Warren C. W. Chan*[,†,∥,⊥]

[†]Institute of Biomaterials and Biomedical Engineering, University of Toronto, 164 College Street, Toronto, Ontario M5S 3G9, Canada

[‡]Stephenson School of Biomedical Engineering, University of Oklahoma, 101 David L. Boren Boulevard, Norman, Oklahoma 73019, United States

[§]Molecular Science and Biomedicine Laboratory, State Key Laboratory of Chemo/Bio-Sensing and Chemometrics, College of Chemistry and Chemical Engineering, College of Biology, Collaborative Innovation Center for Chemistry and Molecular Medicine, Hunan University, Changsha 410082, China

[∥]Departments of Chemistry, Materials Science and Engineering, and Chemical Engineering, University of Toronto, 164 College Street, Toronto, Ontario M5S 3G9, Canada

[⊥]Donnelly Center for Cellular and Biomolecular Research, University of Toronto, 160 College Street, Toronto, Ontario M5S 3E1, Canada

Supporting Information

ABSTRACT: **Coating the nanoparticle surface with cancer cell recognizing ligands is expected to facilitate specific delivery of nanoparticles to diseased cells *in vivo*. While this targeting strategy is appealing, no nanoparticle-based active targeting formulation for solid tumor treatment had made it past phase III clinical trials. Here, we quantified the cancer cell-targeting efficiencies of Trastuzumab (Herceptin) and folic acid coated gold and silica nanoparticles in multiple mouse tumor models. Surprisingly, we showed that less than 14 out of 1 million (0.0014% injected dose) intravenously administrated nanoparticles were delivered to targeted cancer cells, and that only 2 out of 100 cancer cells interacted with the nanoparticles. The majority of the intratumoral nanoparticles were either trapped in the extracellular matrix or taken up by perivascular tumor associated macrophages. The low cancer cell targeting efficiency and significant uptake by noncancer cells suggest the need to re-evaluate the active targeting process and therapeutic mechanisms using quantitative methods. This will be important for developing strategies to deliver emerging therapeutics such as genome editing, nucleic acid therapy, and immunotherapy for cancer treatment using nanocarriers.**

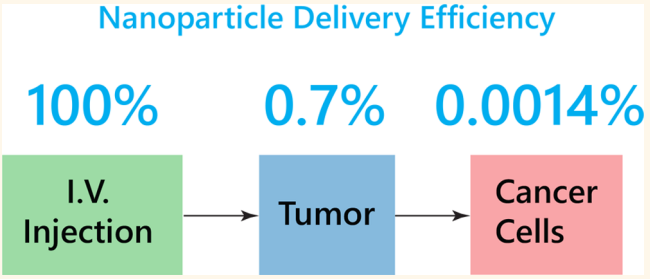

KEYWORDS: *targeting, nanoparticle, flow cytometry, tumor microenvironment, cancer nanomedicine*

Cell specific cancer therapies and diagnostic platforms using nanoparticles have emerged in the last 15 years.[1−4] To reduce nonspecific tissue sequestration and increase blood circulation time, "passive targeting" nanoparticles were coated with a layer of antifouling agents (*e.g.*, poly ethylene glycol (PEG)).[5,6] To increase specific delivery of nanoparticles to cancer cells, researchers coated the nanoparticle surface with biorecognition ligands (*e.g.*, peptides, antibodies, or aptamers) that "actively" target receptors on malignant cells within the diseased tissues.[7−14] This strategy is crucial for delivering cell-specific therapies (*e.g.*, siRNA) to intracellular components (*e.g.*, mitochondria, nucleus) because cargos are often "personalized" and specific to the cell of interest. Improving the cell-targeting efficiency of ligand-coated nanoparticles will be instrumental for the successful translation of emerging technologies such as genome editing, peptide inhibitors, and nucleic acid therapies. The concept of nanoparticle "active targeting" has generated significant interest, based on the steady increase in the number of publications on this topic over the past 10 years (>1500 publications as of 2017, Supporting Information (SI), Figure S1). However, only seven active targeting nanoparticle formulations were in active clinical trials in 2017 (SI, Figure S2).[15]

Received: May 23, 2018
Accepted: July 17, 2018
Published: July 17, 2018

DOI: 10.1021/acsnano.8b03900
ACS Nano XXXX, XXX, XXX–XXX

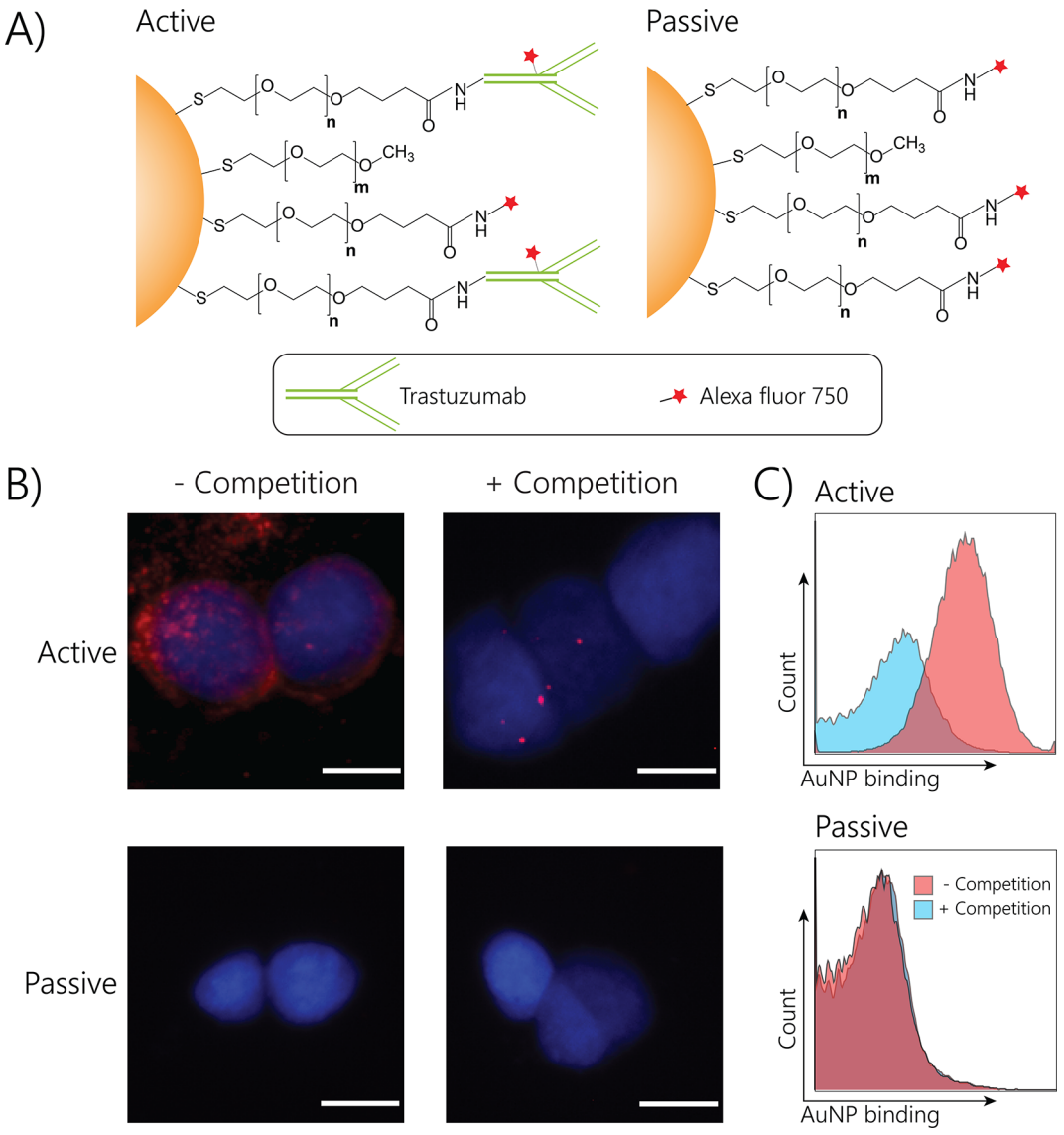

Figure 1. Trastuzumab-conjugated gold nanoparticles (AuNPs) specifically bind to ErbB2(+) cells in vitro. (A) Schematic of surface engineering for active and passive targeting AuNPs. Both designs were decorated on the nanoparticle surface with PEG linkers. (B) Active and passive targeting AuNPs were incubated with fixed SKOV-3 ovarian cancer cells (ErbB2+) in the absence (left two images) and presence (right two images) of excess free Trastuzumab for competition. Cell nuclei were stained with DAPI (blue), while the red signal represents Alexa Fluor 750 (AF750)-labeled AuNPs. (C) Flow cytometry analysis of active and passive targeting AuNPs after incubation with SKOV-3 cells in the presence (blue histograms) and absence (red histograms) of Trastuzumab, respectively. Scale bar = 100 μm.

Conceptually, "active targeting" is an attractive idea, but there are significant challenges in transporting nanoparticles within the tumor. Jain stated in his 1990 review article: "*The efficacy in cancer treatment of novel therapeutic agents such as monoclonal antibodies, cytokines and effector cells has been limited by their inability to reach their target in vivo in adequate quantities.*"[16] Despite this statement, there is little focus on the holistic quantification of nanoparticle transport within the solid tumor. Our 2016 meta-analysis showed that only 0.7% (median) of intravenously administered nanoparticles were delivered to solid tumors,[17] but we suspect that cancer cell targeting efficiency is much lower owing to a number of intratumoral transport barriers. When intravenously administered nanoparticles extravasate from the unevenly distributed and heterogeneous tumor blood vessels, the primary mode of transportation is dependent on the rate of diffusion.[18,19] Here, nanoparticles are often observed to stockpile around the perivascular region and unable to diffuse deep into the tumor space.[18,20−24] The culprit for this inefficient transportation has been pinpointed to tumor interstitial extracellular matrix (ECM), which is composed of collagen, proteoglycan, and glycosaminoglycans. These physical barriers sterically block nanoparticle transport in a size-dependent manner.[25] Active targeting nanoparticles can also interact with perivascular tumor cells, which hinders their ability to diffuse deeper into the tissue.[20,26] Furthermore, various stromal cells within the tumor can also nonspecifically interact with nanoparticles.[27,28] Lastly, high intratumoral interstitial pressure also works counterproductively by limiting nanoparticle transport distance away from the blood vessels.[29,30]

Despite the identification of these barriers, it is unclear to what extent they are hampering nanoparticle targeting to cancer cells. Furthermore, the role of intratumoral cellular barriers (*e.g.*, nonspecific tumor cells) on nanoparticle

DOI: 10.1021/acsnano.8b03900
ACS Nano XXXX, XXX, XXX−XXX

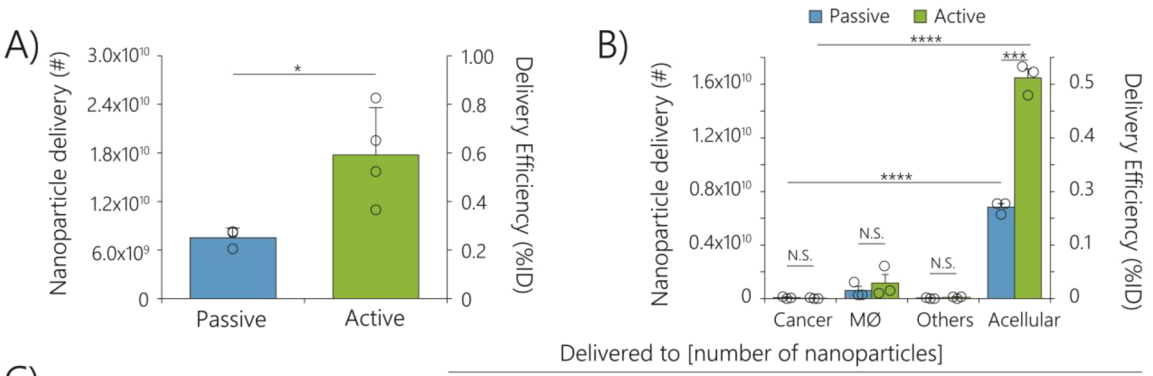

C)

Size [nm]	Surface	Injected dose [#]	Tumour	Cancer	MØ	Other	Acellular
15	Passive	4.00 x 10^{13}	1.8 x 10^{11}	1.1 x 10^{9}	5.0 x 10^{9}	5.0 x 10^{8}	1.7 x 10^{11}
	Active		3.4 x 10^{11}	6.8 x 10^{7}	2.5 x 10^{8}	3.2 x 10^{7}	3.4 x 10^{11}
55	Passive	3.00 x 10^{12}	7.5 x 10^{9}	8.1 x 10^{7}	6.0 x 10^{8}	2.9 x 10^{7}	6.8 x 10^{9}
	Active		1.8 x 10^{10}	2.7 x 10^{7}	1.2 x 10^{9}	9.4 x 10^{7}	1.6 x 10^{10}
100	Passive	9.00 x 10^{11}	1.1 x 10^{8}	0	0	4.4 x 10^{6}	1.1 x 10^{8}
	Active		2.0 x 10^{9}	1.1 x 10^{7}	1.9 x 10^{7}	2.0 x 10^{8}	1.7 x 10^{9}

Figure 2. Quantification of nanoparticles in the tumor microenvironment. (A) Delivery efficiency of active and passive targeting 55 nm AuNPs in SKOV-3 xenograft tumors for 24 h post injection. The quantification of gold content was measured by inductively coupled plasma−mass spectrometry (ICP-MS), and the numbers were normalized to the injection dose (ID). To determine the nanoparticle tumor delivery efficiency, a linear trapezoidal analysis method was used.[17] (B) To determine the nanoparticle delivery efficiency to individual tumor cell populations, the nanoparticles were first intravenously injected into tumor bearing CD-1 nude mice. The whole tumor was dissected and mechanically and enzymatically digested to provide a single cell suspension. Cancer cell and macrophage populations were labeled with EpCAM and F4/80 antibodies, respectively, while the nonlabeled tumor cells were categorized as "others". The acellular region was categorized as contents of the tumor that were not co-pelleted with cells during centrifugation. These tumor portions were then sorted into individual populations *via* fluorescence-activated cell sorting (FACS), and each population was subjected to quantitative ICP-MS analysis of gold content. Accumulation for (B) 55 nm, (C) 15 nm, and 100 nm sized AuNPs in various intratumoral components 24 h post injection. $N = 3-6$, bar graphs represent mean ± SEM. Student's *t* test was used for statistical comparison. N.S. = not significant. *$P \leq 0.05$, ***$P \leq 0.001$, ****$P \leq 0.0001$.

transport is unclear. Without a detailed quantitative analysis of how well "active targeting" works in animal models, current qualitative validation methods (*e.g.*, 2D imaging) will continue to be the gold standard and stymie the development of nanomedicine. Although providing useful information, a major problem of histopathology and optical imaging methods to assess cellular targeting is that they only represent a small portion of the whole tumor. This inspired us to quantify the cellular fate of active targeting nanoparticles in solid tumors. Specifically, we wanted to answer three questions: (i) how many ligand-coated nanoparticles are delivered to cancer cells *in vivo*? (ii) What proportion of intratumoral cancer cells interact with nanoparticles? (iii) Does active targeting improve cancer cell interaction? Quantification of this holistic delivery process will prioritize the intratumoral barriers that need to be eliminated to improve nanoparticle delivery to cells, subsequently correlating cell delivery efficiency to therapeutic responses in future studies. This is an important step in the clinical translation of active targeting nanoparticles.

RESULTS AND DISCUSSION

Receptor Mediated Nanoparticle Binding *in Vitro*. We followed the current research paradigm in demonstrating the targeting of ligand-coated nanoparticles to tumor cells *in vivo*. Researchers typically (1) synthesize and coat nanoparticles with ligands, (2) verify the ligand can target the nanoparticles to cells expressing the complementary receptor to confirm selectivity, and (3) administer this ligand-coated nanoparticle formulation into animals and verify delivery by using end outcome analysis (*e.g.*, imaging for diagnostics and tumor shrinkage or survival studies for therapeutics). We engineered ligand-coated nanoparticles by decorating the surface of gold nanoparticle (AuNPs) with Trastuzumab, an ErbB2 receptor binding antibody. Trastuzumab is a clinically successful, FDA-approved antibody formulation used for breast and ovarian cancer treatment.[8,31−33] The AuNP model system was selected because: (1) AuNPs can be synthesized in a broad size range with narrow size distribution, (2) the number of AuNPs can be precisely quantified using inductively coupled plasma mass spectrometry (ICP-MS) within tissues and cells, and (3) AuNPs allow us to assess the impact of intact nanoparticles on delivery as they do not degrade readily *in vivo*.[32,34,35] Active targeting AuNPs were prepared by surface modification with PEG conjugated to Trastuzumab and fluorescently labeled with Alexa Fluor 750 (AF750).[36] The nanoparticle surfaces were subsequently backfilled with AF750-labeled 5 kDa PEG and methoxy-terminated 2 kDa PEG to minimize protein corona formation while still retaining cancer cell targeting specificity.[37] "Passive targeting" AuNPs were coated with PEG in the absence of Trastuzumab (Figure 1A). We confirmed the successful conjugation of Trastuzumab on the nanoparticle surface *via* protein analysis (SI, Figure S3A). The average nanoparticle hydrodynamic diameter was ∼14 nm larger for Trastuzumab-conjugated nanoparticles in comparison to passive targeting designs (SI, Table S1). The Trastuzumab ligand density was saturated on the surface of AuNP for all three sizes to minimize nonspecific serum protein adsorption.[11] Our nanoparticle designs were stable in mouse serum after 24 hours of exposure (SI, Figures S4,S5). The full characterization

DOI: 10.1021/acsnano.8b03900
ACS Nano XXXX, XXX, XXX−XXX

of physicochemical properties of all AuNP formulations used in this study is summarized in SI, Tables S1,S2, and SI, Figures S3−S6.

Next, we confirmed the specific binding of Trastuzumab-coated AuNPs to ErbB2 cell receptors *via* tissue culture competition assays. We first fixed ErbB2(+) (SKOV-3) and ErbB2(−) (U87-MG) cancer cells (SI, Figure S7) then incubated these cells with Trastuzumab (active targeting) or PEG (passive targeting) coated AuNPs in the presence of excess free Trastuzumab. If the Trastuzumab were successfully conjugated to the AuNPs, the excess free Trastuzumab would have competed for the ErbB2 binding sites and prevent AuNP binding. Fluorescence microscopy images confirmed qualitatively the binding of Trastuzumab-coated AuNPs to ErbB2(+) cells (Figure 1B). In contrast, binding was not observed for ErbB2(−) cells upon incubation with both active and passive targeting AuNPs (SI, Figure S8). We used flow cytometry to quantify the binding specificity of AuNPs to ErbB2 cell receptors (Figure 1C, SI, Figure S9A). The addition of excess Trastuzumab to SKOV-3 cells reduced the AF750 signal up to 60-fold (SI, Figure S9B). This suggests that free Trastuzumab competed with fluorescently labeled Trastuzumab molecules for the ErbB2 receptors on the nanoparticle surface. In contrast, specific binding of passive targeting AuNPs to SKOV-3 cells was not observed. Similarly, there was no specific binding of active and passive targeting AuNPs to ErbB2(−) cells (SI, Figure S9). We concluded that Trastuzumab-coated AuNPs could specifically bind to ErbB2(+) SKOV-3 cells *in vitro*.

Nanoparticle Delivery Efficiency to Tumor Cellular Fractions. Next, we quantified the nanoparticle distribution in the (1) whole solid tumor, (2) cellular/acellular compartments, and (3) different populations of cells using 55 nm AuNPs. This size was chosen because significantly higher cellular interactions compared to nanoparticles with other diameters have been reported in the literature.[38−40] Upon intravenous administration, we quantified the nanoparticle delivery efficiency to solid tumors in human ovarian SKOV-3 xenograft mouse models based on an area-under-the-curve (AUC) analysis method (Figure 2A, SI, Figure S10B). The average nanoparticle-to-tumor delivery efficiency was 0.59% of the injected nanoparticle dose (ID) (or 1.8×10^{10} AuNPs) and 0.25% ID (or 7.5×10^{9} AuNPs) for active and passive targeting nanoparticle designs, respectively (Figure 2A). Similar results had been reported in a recent meta-analysis where median delivery efficiencies were 0.9% ID for active targeting and 0.6% ID for passive targeting nanoparticles.[17] The accumulation in the reticuloendothelial system organs such as the liver was significantly lower for active targeting designs (31.30% ID) than passive targeting designs (62.33% ID) (Figure S11).

Next, we quantified the number of nanoparticles that reached SKOV-3 cancer cells within the solid tumor. We intravenously administered 3.0×10^{12} 55 nm AuNPs into tumor-bearing CD1 nude mice. At 24 h post injection (HPI), subcutaneous xenograft tumors were excised and digested by mechanical and enzymatic breakdown to give single cell suspensions. SKOV-3 cancer cells and tumor associated macrophages (TAMs) were then immuno-labeled using fluorescent antihuman EpCAM and antimouse F4/80 antibodies, respectively. Cells that were not labeled by these antibodies were considered as "other" nonmalignant cell types. Immuno-labeled single-cell suspensions were then subjected to fluorescence-activated cell sorting (FACS), and the sorted populations were quantified by ICP-MS to obtain the average number of nanoparticles (SI, Figure S12). Only 0.001% ID (2.7×10^{7} AuNPs) of active and 0.003% ID (8.1×10^{7} AuNPs) of passive targeting nanoparticles interacted with SKOV-3 cells (Figure 2B,C). In other words, nine out of a million administered 55 nm Trastuzumab-coated nanoparticles reached cancer cells. We found no statistical difference in the cancer cell interactions between active and passive targeting nanoparticles, which indicates that nanoparticle binding to these cells was nonspecific. In contrast, an average of 0.038% ID (1.2×10^{9} AuNPs) of active or 0.020% ID (6.0×10^{8} AuNPs) of passive targeting nanoparticles were observed in TAM populations (Figure 2B,C). This demonstrates that nanoparticles were 7−38 times more likely to interact with TAMs rather than cancer cells. Since only ∼10% of intratumoral nanoparticles were associated with cells, we wondered where the other ∼90% of nanoparticles resided. To answer this question, we quantified the number of AuNPs in the acellular component of the digested tumor by using ICP-MS. We verified that the digestion process did not remove nanoparticles from cell surfaces (SI, Figure S13) nor did the nanoparticles cause a significant reduction in cell metabolic activities (SI, Figure S14). This suggests that we did not quantify a biased cell population after nanoparticles interacted with cells. We found that out of the 0.59% ID (1.8×10^{10} AuNPs) of intratumoral active targeting nanoparticles, 0.55% ID (1.6×10^{10} of AuNPs) were in acellular regions. Similarly, out of the 0.25% ID (7.5×10^{9} AuNPs) of intratumoral passive targeting AuNPs, 0.23% ID (6.8×10^{9} AuNPs) were in acellular regions (Figure 2B,C). Furthermore, we wondered if the low cancer cell targeting could be due to the loss of Trastuzumab molecule on the AuNP during circulation. To confirm that the Trastuzumab were still on the nanoparticle surface in the tumor microenvironment, we imaged histology slices of tumors and found colocalization of Trastuzumab molecules with nanoparticle signals (SI, Figure S15).

We further analyzed the impact of nanoparticle size in driving receptor mediated binding to cells *in vivo*. We studied the active targeting of both 15 and 100 nm AuNPs. Similar to 55 nm AuNPs, accumulation of 15 and 100 nm AuNPs in TAMs and other nonmalignant cells were 4.1−19.4 times higher than for cancer cells (Figure 2C, SI, Figure S12). Across all three AuNPs sizes, we observed that 88.2−99.9% of Trastuzumab-coated nanoparticles resided in acellular regions of the tumor at 24 h (SI, Figure S12). The reason for low delivery efficiency of small and larger nanoparticles to tumor cells are potentially different. Even though 15 nm AuNPs have had deeper tumor penetration,[21,41] these nanoparticles may need to cluster together for efficient cellular uptake (SI, Figure S16).[38] If Trastuzumab-coated nanoparticles were not available at a high enough number to enable clustering on the cell membrane, they would not be internalized efficiently. The 100 nm nanoparticles did not penetrate deep into the tumor to reach the cancer cells, as their diffusion rate was restricted by the ECM.[21] The ECM in the acellular region had been discussed in the past as major steric barriers for the transport of larger nanoparticles,[18] hence 100 nm AuNPs may not reach or interact with cancer cells. The signal was below the detection limit for the ICP-MS technique. These results demonstrated that within a solid tumor, acellular regions and TAMs constituted the biggest barriers to cancer cell targeting, as they sequestered >88.2% of extravasated nanoparticles.

DOI: 10.1021/acsnano.8b03900
ACS Nano XXXX, XXX, XXX−XXX

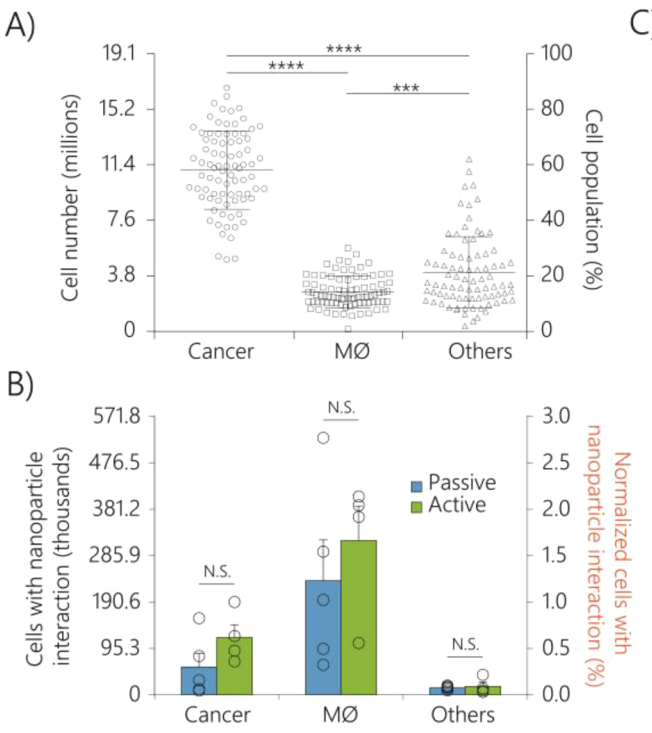

C)

Normalized cells with nanoparticle interaction [%]

NP	Ligand	Tumour	Size [nm]	Surface	Cancer	MØ	Others
Gold	Trastuzumab	SKOV-3 [ErbB2+]	15	Passive	0.02	0.29	0.01
				Active	0.24	0.16	0.01
			55	Passive	0.30	1.23	0.08
				Active	0.62	1.66	0.09
			100	Passive	0.14	0.25	0.07
				Active	0.03	0.06	0.01
		U87-MG [ErbB2-]	15	Passive	0.16	0.36	0.36
				Active	0.41	0.24	0.10
			55	Passive	0.35	1.01	0.22
				Active	0.03	0.36	0.07
			100	Passive	0.05	0.76	0.16
				Active	0.10	0.09	0.08
		Calu-3 [ErbB2+]	55	Passive	0.60	0.02	2.05
				Active	0.20	0.01	1.41
	Folate	4T1 [Folate receptor+]	15	Passive	0.13	4.00	0.38
				Active	0.00	0.05	0.07
			55	Passive	0.39	4.97	1.53
				Active	0.04	0.97	0.25
			100	Passive	0.01	0.05	0.03
				Active	0.00	0.11	0.09
Silica	Trastuzumab	SKOV-3 [ErbB2+]	100	Passive	0.00	0.12	0.01
				Active	0.01	0.03	0.00
			140	Passive	0.00	0.02	0.00
				Active	0.01	0.05	0.01

Figure 3. Quantification of intratumoral nanoparticle-cell interactions. (A) Flow cytometry quantification of cell populations in SKOV-3 xenograft tumors. Intact, singlet population of cancer, macrophage, and other cells from each tumor were collected and normalized to 100% of the cell population. N = 83. (B) Binding of 55 nm AuNPs to cancer, macrophage, and other cell populations at 24 h post injection in SKOV-3 tumors. The y-axis values were normalized to the total cells within the tumor as opposed to the cells within each phenotype population (*e.g.*, cancer). (C) Summary of nanoparticle−cell interactions in SKOV-3, U87-MG, Calu-3, and 4T1 tumors models with either Trastuzumab or folate as targeting ligands. The percentage were calculated in relation to the total number of cells in the tumor as opposed to each individual cell population. N = 3−6, bar graphs and whisker plots represent mean ± SEM. Student's t test was used for statistical comparison. ***$P \leq 0.001$, ****$P \leq 0.0001$.

Proportion of Tumor Cells that Interact with Nanoparticles. To elucidate the next hierarchical level of nanoparticle interaction in the tumor microenvironment, we quantified the cell−nanoparticle interactions using flow cytometry. As oppose to observing AuNP accumulation in the whole tumor, here we examined the proportion of tumor cells that interact with AuNPs. Single cell suspensions from tumor disaggregation were gated for singlet cells and intact cells to exclude debris signals (SI, Figure S17). We first identified cancer cells and macrophages using antihuman EpCAM and antimouse F4/80 antibodies, respectively. Their identities were further confirmed via dual-marker labeling and aneuploidy analysis for multiple copies of DNA (SI, Figures S18,S19). We then estimated the average number of cells per tumor using flow cytometry. This was calculated by excluding the debris population that originated from necrotic areas and the dead cells (smaller than the size of a cell, SI, Figure S17A), doublet population (cells that are stuck together, SI, Figure S17B), and intact cells (stained by DAPI, SI, Figure S17C). The number was then extrapolated based on the proportion of sample used for flow cytometry relative to whole tumor. The number of nondebris, singlet, and intact cell population per tumor was approximately 19.1 × 10^6 (SI, Figure S20). Within this number, SKOV-3 cells constituted 11.1 × 10^6 cells (58.1% of the population), TAM constituted 2.7 × 10^6 cells (14.2%), and "other" unidentified cells constituted 5.2 × 10^6 cells (27.3%) (Figure 3A). At 24 HPI, only 0.11 × 10^6 cells (0.96%) and 0.05 × 10^6 cells (0.42%) out of 11.1 × 10^6 SKOV-3 cells interacted with active and passive targeting 55 nm AuNPs, respectively (SI, Figure S21). The difference in SKOV-3 cells interaction was insignificant for active and passive targeting nanoparticles (Figure 3B), suggesting that some of these interactions may be nonspecific. These data corroborated the results from our ICP-MS analysis. Comparing to cancer cells, a larger proportion of the TAM population interacted with nanoparticles. Out of 2.7 × 10^6 TAMs, 55 nm AuNPs interacted with 0.36 × 10^6 cells (13.26%) and 0.34 × 10^6 cells (12.48%) for active and passive targeting designs, respectively (SI, Figure S21). Analysis at longer time point (48 HPI) also showed poor cancer cell targeting, where TAMs and other cell populations dominated nanoparticle interaction (SI, Figure S22). We also measured the relative amount of fluorescence per cell within each of the cell populations and found that TAMs took up 1.6−2.1 more nanoparticles per cell than cancer cells or other cells (SI, Figure S23). These results were in line with studies by Weissleder *et al.*[27,42] We also performed similar analysis with 15 and 100 nm AuNPs to assess the nanoparticle size-dependent effect. Unlike the 55 nm counterpart, the total percentage of cells that interacted with 15 and 100 nm AuNPs were 3.5−24.2 times lower at 24 HPI. Irrespective of the presence of the targeting ligand on the nanoparticle surface, the majority of these cellular interactions were dominated by TAMs (SI, Figure S21D,F). These results demonstrated that TAMs are the first major cellular barrier after extravasation from the vessel that prevents active targeting nanoparticles from reaching cancer cells.

Effect of Tumor Composition and Material on Nanoparticle Distribution. To ensure that our observations

DOI: 10.1021/acsnano.8b03900
ACS Nano XXXX, XXX, XXX−XXX

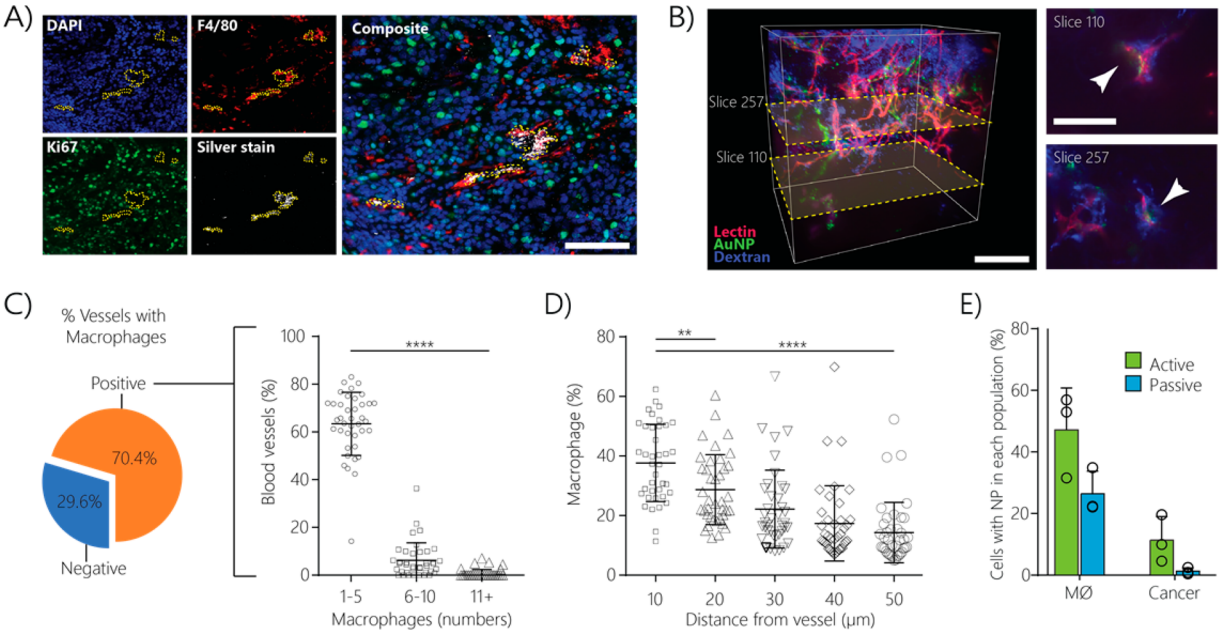

Figure 4. Spatial sequestration of nanoparticles by tumor associated macrophages (TAMs). (A) SKOV-3 xenograft tumor histology slice from CD-1 nude mice were stained for DAPI, F4/80, Ki67, and silver for the presence of cell nuclei, macrophage, cancer cells, and 55 nm active targeting nanoparticles, respectively. (B) Three-dimensional image of SKOV-3 xenograft tumor processed by the CLARITY tissue clearing method. CD-1 nude mice bearing SKOV-3 xenograft tumor were intravenously injected with Lectin−Alexa fluor 555 and dextran−Cy5 prior to sacrifice to stain for blood vessels and TAMs, respectively. Arrows represent the colocalization of 55 nm active targeting AuNPs and dextran. (C) The percentage of blood vessels in each histology image were then classified and binned for the presence of perivascular macrophage (see method for detailed description). (D) Histology image quantification of macrophage proportion in respect to distance away from blood vessel. The percentage of TAMs within 50 μm from the blood vessel were quantified using a MATLAB algorithm, which recognizes the fluorescence blood vessel outline and radially expands outward to form concentric rings. (E) *In vitro* evaluation of nanoparticle diffusion in 3D Matrigel coculture with fluorescently labeled SKOV-3 (cancer) and Raw264.7 (macrophage) cells. The microchannel were first infused with 25% v/v Matrigel, while the either end of the channel were left empty. Nanoparticles were introduced into the reservoir on one end and allowed to diffuse through the microchannel setup. The percentage of SKOV-3 and Raw264.7 cells with AuNP binding were quantified in the graph. Scale bars: (A) 100 μm; (B) 300 μm in the larger image, 150 μm in the slice images; One-Way ANOVA was used for statistical comparison. $^{**}P \leq 0.01$, $^{****}P \leq 0.0001$. $N = 39$ for C,D, while each n represents one field of view of 1 mm × 1 mm. $N = 3$ for E.

were not exclusive to human ovarian SKOV-3 xenograft tumors, we evaluated other (1) tumor models, (2) targeting ligand, and (3) nanomaterial composition. AuNP formulations were first tested on human glioblastoma U87-MG (ErbB2-) and human lung adenocarcinoma Calu-3 (ErbB2+) xenograft tumor models. The under- and overexpression of the ErbB2 receptor in these two tumor types provided control conditions for the quantification of Trastuzumab-conjugated nanoparticle targeting efficiency. As expected for ErbB2- tumor (U87-MG xenograft model), Trastuzumab-conjugated active targeting nanoparticles did not significantly accumulate more in cancer cells compared to passive targeting nanoparticles (SI, Figure S24). Similar results were also observed for ErbB2+ Calu-3 tumors (SI, Figure S25). In both tumor models, most nanoparticles accumulated in TAMs and other cells, thus outcompeting their cancer cell counterparts.

Next, we evaluated targeting capabilities of folate-conjugated-nanoparticles in orthotopic syngeneic mouse breast tumor model (4T1 cells). First, we evaluated the binding specificity of our folate conjugated nanoparticles *in vitro via* a dose escalation binding study (SI, Figure S26). Upon intravenous administration, we found that macrophages were still the dominant cell type that took up active and passive targeting nanoparticles across three different nanoparticle sizes. Furthermore, the presence of folate on the nanoparticle surface did not significantly improve cancer cell delivery efficiency (SI, Figure S27). This is in line with our results obtained from Trastuzumab-coated AuNPs in SKOV-3 tumors.

To examine whether results observed for AuNPs also applied to other nanoparticle materials, we further evaluated two sizes (100 and 140 nm) of silica nanoparticles (SiNPs). Trastuzumab ligands were covalently conjugated to SiNPs and showed similar patterns as AuNPs in terms of delivery and targeting capabilities. Results obtained using SiNPs confirmed that the low nanoparticle delivery efficiencies to SKOV-3 cells observed for AuNPs were not due to ligand desorption from these nanoparticles (Figure 3C, SI, Figure S28). Similar to AuNPs, SiNPs interacted with TAMs 2.7−31.9 times more than cancer cells (SI, Figure S29).

TAMs Spatial Localization Favors Nanoparticle Interaction. Thus far, our data quantitatively concluded that TAMs dominated nanoparticle uptake even in the presence of targeting ligands. We further confirmed this conclusion by using 2-dimensional immunofluorescent histopathology analysis (Figure 4A) and 3-dimensional optical imaging of tissue-cleared samples (Figure 4B). In all of these images, we observed colocalization of AuNPs with TAMs. Our images showed that TAMs surround tumor blood vessels (SI, Figure S30). To quantify this, we developed an algorithm to automatically calculate the proportion of perivascular TAMs versus other cells (*e.g.*, cancer cells, other cells) surrounding tumor blood vessels on immunofluorescent histology samples.

DOI: 10.1021/acsnano.8b03900
ACS Nano XXXX, XXX, XXX−XXX

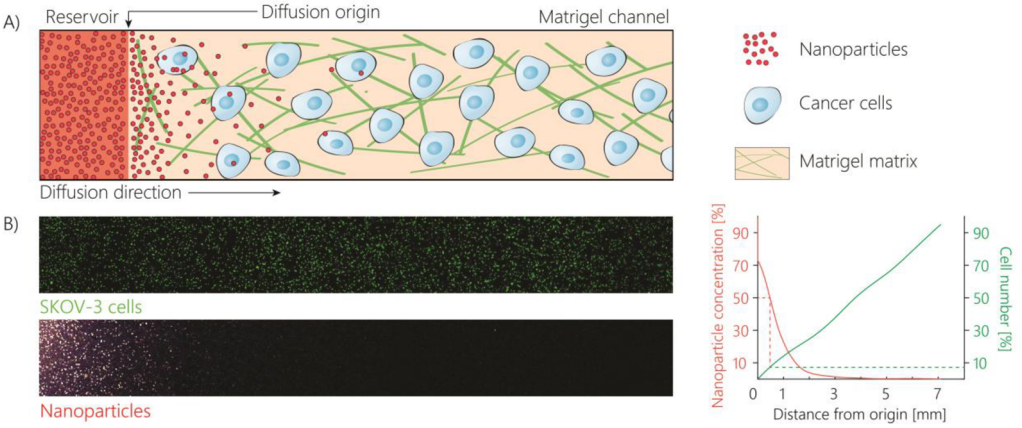

C)

Parameter	Material	Size [nm]	Ligand	Corona	Matrigel [%]	Diffusion distance [μm]	Cells accessed [%]
Size	Gold	15	Herceptin	No	25	383.0	7.5
	Gold	55	Herceptin	No	25	195.9	3.1
	Gold	100	Herceptin	No	25	0.0	0.0
	Gold	15	Cy5	No	25	640.1	7.5
	Gold	55	Cy5	No	25	527.1	5.0
	Gold	100	Cy5	No	25	189.2	2.2
Protein corona	Gold	55	Cy5 (Low)	Yes	25	0.0	0.0
	Gold	55	Herceptin	Yes	25	0.0	0.0
Ligand	Gold	55	Folate	No	25	0.0	0.0
	Gold	55	Albumin	No	25	0.0	0.0
	Gold	55	Transferrin	No	25	129.6	1.9
Material	Silver	50	PEG	No	25	276.3	5.1
	Silver	100	PEG	No	25	0.0	0.0
	PLGA	100	PEG	No	25	472.2	7.5
	QD	5	PEG	No	25	223.1	3.9
	Liposome	100	PEG	No	25	0.0	0.0
Matrigel % v/v	Gold	55	Herceptin	No	12.5	389.8	4.8
	Gold	55	Herceptin	No	50	0.0	0.0
	Gold	55	Herceptin	No	75	0.0	0.0
Control	Cy5	<1	N/A	No	25	1205.6	23.9
	Herceptin	~8	N/A	No	25	933.5	18.1
	Bead	200	PEG	No	25	0.0	0.0

Figure 5. ECM impedes nanoparticle access to cancer cells in *in vitro* Matrigel model. (A) Schematic of the *in vitro* evaluation of nanoparticle diffusion in 3D Matrigel culture with SKOV-3 cells for 24 h. (B) Representative confocal images and quantification of nanoparticle diffusion distance and the amount of SKOV-3 cells it could access. The diffusion distance was denoted as 50% of the initial nanoparticle concentration away from the reservoir (orange line). The corresponding distance also reflected the percentage of cells the nanoparticles had access to (green line). (C) Average values depicting the diffusion distance and the percentage of cells the nanoparticles had access to for various design criterion. Unconsolidated raw data presented in the table can be found in SI, Figures S35−S38.

The algorithm recognized the outline of blood vessel based on fluorescence labeling of the lumen wall and then expanded radially outward to estimate the number of TAMs and other cells that meet the blood vessel (SI, Figure S31A). We found that 70.4% of tumor blood vessels had perivascular TAMs, and most of these vessels had 1−3 TAMs in the surrounding periphery (Figure 4C). Additionally, the proportion of TAMs decreases from 37.7% in the first 10 μm away from the blood vessel to 14.3% 50 μm away from the blood vessel (Figure 4D, SI, Figure S31B). These data suggest that TAM concentration was highest near the blood vessel. In other words, nanoparticles would have a high probability of first interacting with TAMs upon extravasation from tumor blood vessels before interacting with other cells. The majority of nanoparticles did not diffuse far into the ECM, thus nanoparticles were within accessible range of these perivascular macrophages (Figure 4D, SI, Figure S32−S33).

Next, we developed an *in vitro* Matrigel model to demonstrate two principles: (1) macrophages are competitive in nanoparticle uptake and (2) ECM prevents deep penetration and interaction of ligand-coated nanoparticles with cancer cells. Both biological barriers could limit interactions of AuNPs with cancer cells, leading to differential uptake between the TAMs and cancer cells.

We co-cultured SKOV-3 cancer cells and Raw264.7 murine macrophages in Matrigel to mimic the two cell types in the intratumuoral microenvironment in a microchannel system (Si, Figure S34). Because we observed the highest cellular interaction for 55 nm AuNPs, they were introduced into one end of the channel reservoir. At 24 h after administration, we quantified the percentage of cells within each cell population that were positive for nanoparticle fluorescence signal. For the active targeting nanoparticles, 47.1% of the macrophage population were nanoparticle positive, while only 11.4% of the cancer cell population were nanoparticle positive (Figure 4E). This suggests that when nanoparticles encountered cells during diffusion, macrophages were more favorable to take up

DOI: 10.1021/acsnano.8b03900
ACS Nano XXXX, XXX, XXX−XXX

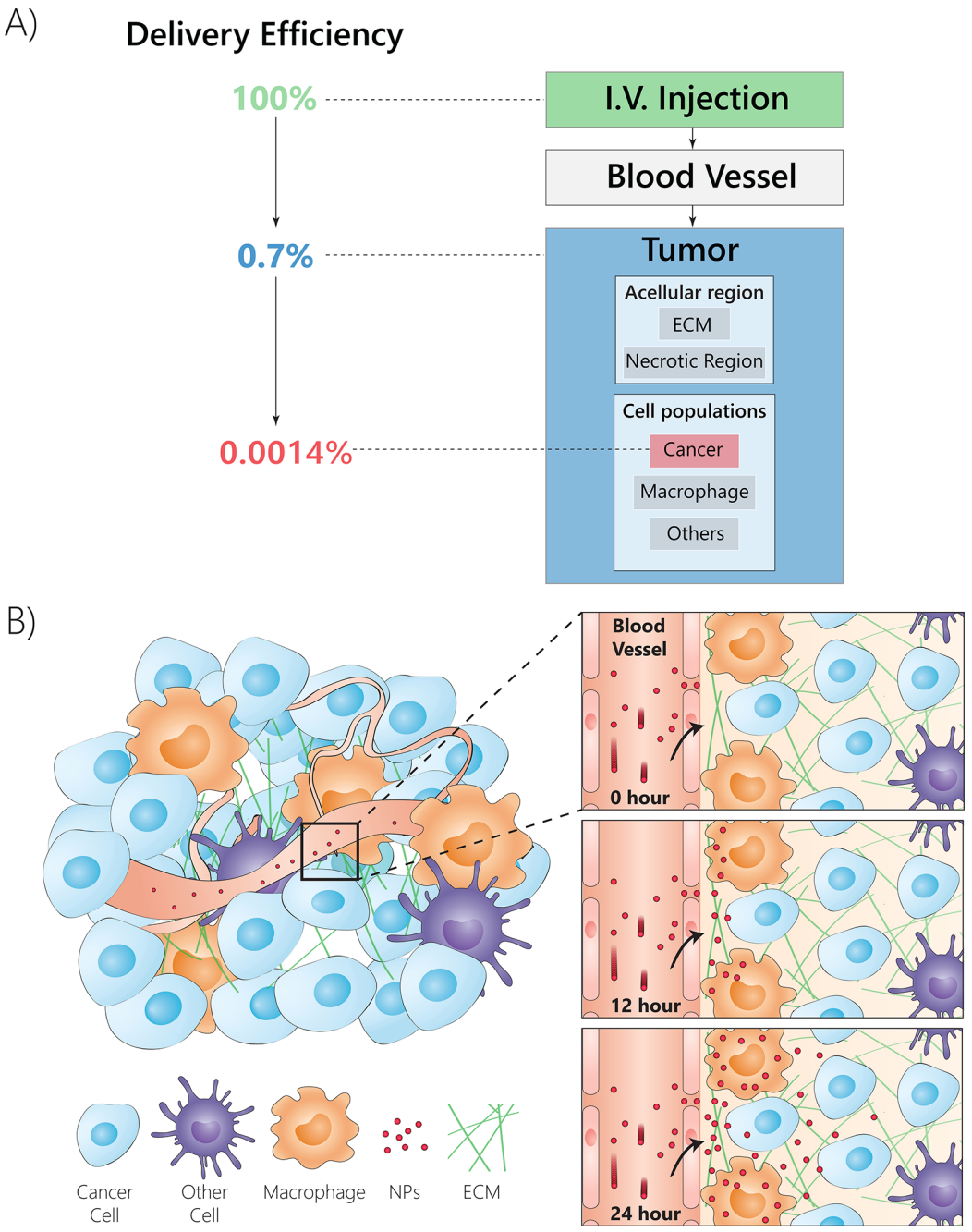

Figure 6. Nanoparticle acellular and cellular sequestration in the tumor. (A) Holistic view of nanoparticle transport because the point of injection to its intratumoral fate in the cellular and acellular regions. (B) Upon extravasation from the tumor blood vessels, nanoparticles are sterically blocked by the extracellular matrix. The short traveling distance of the nanoparticles favors nanoparticle interaction with perivascular TAMs, due to their high concentration near the blood vessels, and their intrinsic propensity to take up nanoparticles.

nanoparticles due to their phagocytic nature. Phagocytic cells could reduce the availability of NPs for cancer cell targeting.

To test the effect of the extracellular matrix on nanoparticle diffusion, we measured how far nanoparticles were able to diffuse using a tissue culture tumor transport model and quantified the percentage of cells these nanoparticles had access to. We tested 17 distinct nanoparticle formulations to demonstrate a broad analysis of these transport characteristics. All tested nanoparticle designs, including targeting and nontargeting, hard and soft nanomaterials, as well as nanomaterials with and without protein corona, exhibited exponential decay in diffusion distance in the microchannel reservoir. The results showed that <8% of the cells were accessed by nanoparticles (Figure 5, SI, Figures S35–S38). This is in line with our flow cytometry data where <3% of total tumor cells interacted with nanoparticles (Figure 3). We further examined the effect of matrix composition in mediating transport to reach the cells. All tested Matrigel concentrations stymied nanoparticle diffusion and reduced access to cancer cells (SI, Figure S38). These results showed that ECM could hinder the penetration of the nanoparticles and lower the probability of interactions between nanoparticles and cancer cells.

DOI: 10.1021/acsnano.8b03900
ACS Nano XXXX, XXX, XXX−XXX

Evaluation of Cell-Specific Toxicity. The low delivery efficiency of AuNPs to targeted cancer cells begs the question of why many previous studies on nondegradable therapeutic nanoparticles showed tumor shrinkage or increased survival in mouse tumor models. Answering this question would require direct correlation between cancer cell targeting efficiency and therapeutic efficacy *in vivo*. Currently this cannot be done because there is no strategy to control and fine-tune the cell targeting efficiency *in vivo*, therefore this idea will be pursued in future work. We hypothesized that tumor shrinkage seen in other studies was due to indiscriminate killing of stromal and cancer cells alike. To demonstrate this, we designed an *in vitro* co-culture (SKOV-3 and Raw264.7 cells) experiment. *In vitro* cell culture experiments remove a majority of biological barriers (*e.g.*, liver clearance, nonspecific accumulation, etc.) that would hinder the transport of the nanoparticles to the cancer cell. As a result, these experiments allowed us to directly assess the impact of nanoparticle cancer cell delivery efficiency on therapeutic response. Trastuzumab−doxorubicin−AuNPs (active targeting) or doxorubicin−AuNPs (passive targeting) with a nanoparticle size of 55 nm were synthesized as a model payload-nanoparticle system (SI, Figure S39). For active targeting nanoparticles, we observed cell death in both cancer cells (0.4%) and macrophage (3.6%) populations (SI, Figure S40C). When we increased the nanoparticle dose by 10× as a surrogate to increased cell targeting efficiency, we observed a surprising increase in the macrophage cell death (34.3%) but not in the cancer cell (0.0%) population (SI, Figure S40E). Together with the previous data, we concluded that the high phagocytic nature of TAMs as well as their spatial location make it favorable for taking up active targeting nanoparticles. Consequently, this indiscriminate toxicity in macrophages may be why researchers observed tumor size reduction data in active targeting nanoparticle formulations. Further evaluation of the role of killing TAMs in mediating animal survival is required to understand the consequences of the low tumor cell targeting.

DISCUSSION

Nanoparticles have been proposed as delivery vehicles that can shuttle therapeutic agents to solid tumors and cancer cells. Our recent literature survey showed that only 0.7% (median) of systemically administered nanoparticles are delivered to solid tumors in preclinical animal models. This prompted us to inquire the fate of administered nanoparticles after they have reached the soild tumor. Specifically, we were interested in exploring whether the targeting ligands on nanoparticle surface can drive its accumulation in cancer cells. To address these questions, we designed a Trastuzumab coated nanoparticle that can minimize serum protein adsorption while retaining targeting specificity to ErbB2 receptors on cancer cells *in vitro*.[37] In this paper, we showed that <14 out of the 1000000 administered Trastuzumab-coated gold nanoparticles were interacting with cancer cells in tumors, while up to 90% of the cell-bound nanoparticles were taken up by TAMs (Figure 6). The low cancer cell targeting and dominant TAM sequestration signifies that other stromal cells compete for nanoparticles within the tumor.[27,28,42,43] Miao *et al.* showed high tumor associated fibroblast (TAF) uptake of lipid-coated calcium phosphate nanoparticles in a xenograft tumor model, which was generated through a mixture of 3T3 fibroblast and UMUC3 cancer cells. In this particular animal model, the 3T3 cells artificially inflated the TAF population within the tumor, providing more noncancer cells to compete with the cancer cells for nanoparticles. As a consequence, the authors observed a 7× difference between nanoparticle uptake by nonspecific TAF compared to other cells (including cancer cells). While Miao *et al.* showed elevated TAF population in the tumor, most nondesmoplastic models (like the ones in our study) have a lower number of fibroblast cells in the solid tumor. As a result, we did not observe high nanoparticle uptake into the fibroblast population. There are also contrasting data presented in other studies. Kirpotin *et al.* showed that anti-Her2 Fab conjugated liposomes accumulated in cancer cells 4.1× more likely than murine host cells. The issue with liposomes is that they are prone to *in vivo* degradation, meaning that the signal can come from either intact nanoparticles or its constituents. Without the ability to decouple a nanoparticle from its components, it would be difficult to conclude the targeting efficiency of active targeting nanoparticles. Aside from dominant nanoparticle uptake by cellular components such as the TAM, we also observed a high sequestration of nanoparticles in the acellular region of the tumor. We believe that the ECM is responsible for the majority of this sequestration, mainly because of its high density near tumor blood vessels.[34] Although they had been identified as a barrier to nanoparticle transport, the extent of nanoparticle sequestration is unknown prior to this paper. Nevertheless, our study and prior studies clearly showed the competitive intratumoral landscape for extravasating nanoparticles within the solid tumor. Future studies examining various types of targeting ligands in diverse sets of tumor subtypes will be required to obtain a full picture of how intratumoral biological barriers hinder active targeting. To ensure that nanoparticles can target cancer cells effectively, we will need to (1) understand how tumor biology influences nanoparticle transport and (2) develop strategies to "tip" the nanoparticle delivery efficiency in favor of the cancer cells.

Nanomedicine translation is hinging on the mechanistic understanding of nanoparticle fate in the tumor. As of now, the pathway of active targeting in an *in vivo* system is still unclear. The purpose of our study was to quantify the nanoparticle delivery process from a whole tumor perspective down to the cellular level. This kind of quantification has direct ramifications on how research will be performed in the future. Currently in the academic community, active targeting is typically characterized by (1) *in vitro* cell culture studies (mitigates the issue of tumor complexity and barriers), (2) histopathology analysis (distribution throughout the whole tumor tissue is not accounted for), and (3) end-outcome measurements such as mouse survival or tumor size shrinkage. Many researchers had clearly demonstrated that ligand-coated nanoparticles carrying cancer agents (siRNA, chemotherapeutics) are capable of decreasing tumor size and improve animal survival. There is a disconnect between our observation of low cancer cell targeting efficiency via flow cytometry, poor nanoparticle accessibility *via* imaging, and the reported final therapeutic outcome. However, direct quantitative analysis of active targeting *in vivo* has rarely been conducted in these studies. We hypothesize several possibilities for the reported therapeutic outcomes of active targeting: (1) the nanoparticle degraded and released the therapeutic agent in the tumor site which would diffuse into the cancer cells,[44] (2) there could be indiscriminate cell killing (cancer cells and stromal cells alike) in the tumor, which could lead to shrinkage and prolonged survival, and (3) there could be a "bystander effect," where the

DOI: 10.1021/acsnano.8b03900
ACS Nano XXXX, XXX, XXX−XXX

death of few cancer cells produce chemical signals that that kills nearby cells. These suggested possibilities are only speculation as we do not have corresponding tissue samples for further analysis. Once we develop methods to quantitatively assess and control the delivery process, we can fully address the therapeutic relationship with cancer cell targeting efficiency. Elucidating this correlation will provide further insight into improving therapeutic efficacy of nanomedicine.

Aside from developing a deep understanding of nanoparticle transport within the tumor microenvironment, the research community could benefit from strategies that can circumvent the barriers that we have discussed in this study. TAM depletion had been explored in the past using bisphosphonate clodronate liposomes.[45,46] Ongoing studies by Roche using CSF1R inhibitor are currently undergoing clinical trials.[47] On the ECM front, enzymes that degrade ECM components such as collagen[25] and hyaluronan[48] have also been suggested. Thus far, these strategies have been suggested as stand-alone therapies. It would be interesting to see whether these treatments would open more opportunities for nanoparticle targeting to cancer cells in coinjection or sequential injection schemes. The quantification of cancer cell targeting provides a reference point for the field to compare and contrast these methods.

Lastly, it is important for the field to define the term "active" targeting in the context of TAM presence. The rationale behind "active" targeting using a cell-specific ligand is to improve cell-specific accumulation in the tumor. If "active" cancer cell targeting nanoparticles accumulate in higher proportion in nonspecific cell types such as TAMs, then current strategies of designing "active" targeting nanoparticles are flawed. Although previous studies[27,42] have shown that cargos from therapeutic nanoparticles could be released subsequent to macrophage uptake, these nanoparticles were not functionalized with cancer cell targeting ligands. If the mechanism of action for "active" targeting nanoparticles is explained via the macrophage reservoir effect, it is a coincidental side effect as opposed to rational design. This downplays the definition of "active" targeting.

CONCLUSION

The tumor is a complex organ where cancer cells have built an environment to protect and support their activity. The idea of using a ligand to overcome these protective barriers is too simplistic. Developing viable treatment strategies requires a more detailed understanding of fate and behavior of nanoparticles inside the tumor. In our study, we found that <14 out of 1 million administered Trastuzumab-coated nanoparticles reached the cancer cell population within solid tumors in preclinical mouse models. This poor performance was facilitated by intratumoral cellular and acellular barriers. Moving forward, a central objective of cancer nanomedicine should be focused on overcoming or manipulating these barriers to improve the therapeutic response. Identifying and segmenting various mechanisms for tumor reduction would also allow the field to prioritize important intratumoral cellular or acellular targets. Here, quantification of targeting efficiency and correlation to therapeutic efficacy would allow us to evaluate the success of these efforts as it serves as a comparison between different strategies. Our proposed quantification and analysis scheme provides a first step in understanding the intratumoral fate of nanomaterials. Further studies are required to provide a complete picture of intratumoral barriers that impede active targeting. Once that occurs, new strategies could be created to overcome these barriers to improve the clinical translation of active targeting nanoparticles for treating solid tumors.

METHODS

Tumor Disaggregation and Antibody Labeling. Resected tumors were first mechanically sliced using razor blades to produce <2 mm fine fragments. The dissected tumor fragments were placed into 5 mL of 1× HBSS buffer with 0.4 mg/mL collagenase IV and 0.02 mg/mL DNase I. The enzymatic digestion process was allowed to occur for 90 min at 37 °C under rotation. The single cell suspension produced from the previous process was filtered using a 100 μm cell strainer to remove undigested tissue and cellular aggregates. The filtrate was centrifuged at 300*g* for 10 min at 4 °C, followed by the removal of the supernatant. To remove red blood cells, 2 mL of red blood cell (RBC) lysis buffer were added to the cell pellet and incubated on ice for 5 min, followed by centrifugation at 300*g* for 10 min at 4 °C. The cells were washed 2 more times at 300*g* for 10 min using 1× HBSS buffer supplemented with 0.5% w/v BSA and 2 mM EDTA. Cell concentrations were roughly estimated using Trypan Blue count by an automated Vi-Cell instrument (Beckman Coulter). Before antibody labeling, all samples were adjusted to 100 μL of 65 × 10^6 cells/mL for regular flow cytometric measurements, and 1800 μL of 65 × 10^6 cells/mL for fluorescence assisted cell sorting. For the regular flow cytometry samples, 5 μL of stock EpCAM, 2 μL of stock F4/80, and 2 μL of stock CD16/32 were added to the cells and mixed gently. All of the antibody volumes were linearly scaled up 18× for samples prepared for fluorescence assisted cell sorting. The antibody labeling was performed at 4 °C on ice for 30 min in the dark. Following antibody labeling, the cells were stained with 10 μL of 0.1 mg/mL DAPI in 1× PBS in the presence of 0.1% saponin for 30 min at room temperature in the dark. The cells were subsequently washed three times with 1× HBSS at 300*g* for 10 min at 4 °C. The cells were resuspended in 500 μL of 1× HBSS, followed by the addition of equal volumes of 4% paraformaldehyde in 1× HBSS buffer on ice for 30 min. Upon fixation, cells were washed three times at 300*g* for 10 min at 4 °C using 1× HBSS supplemented with 0.5% w/v BSA and 2 mM EDTA.

Flow Cytometry and Fluorescence Assisted Cell Sorting (FACS). Before cell sorting, samples prepared from tumor single cell suspension were filtered through a 100 μm cell strainer to remove large aggregates. The filtrates were subjected to regular flow cytometry using BD Fortessa or FACS using BD Influx cell sorter located in the Flow Cytometry Facility in the Medical Science Building, University of Toronto. The settings used for flow cytometry on BD Fortessa are described in SI, Tables S7,S8.

Quantification of Nanoparticle Accumulation in Organs Using Elemental Analysis. Samples were first digested in acid by using 1 mL of aqua regia (1 part nitric acid, 3 parts hydrochloric acid) at 70 °C in a water bath for 6 h. Samples were spiked with 1 μg/mL of yttrium(III)chloride to act as an internal standard. Upon digestion, the samples were passed through a 0.22 μm PES filter to eliminate large debris that could interfere with inductively coupled plasma (ICP) elemental analysis. All measurements for total tumor accumulation were done using Optima 7300 ICP optical emission spectroscopy (OES) machine in the ANALEST facility, University of Toronto. For FACS sorted samples and nontumor organs, PerkinElmer Nexion 350D located in MaRS Discovery District (NanoMedFab), Toronto, was used for ICP-mass spectrometry (MS) measurements.

Chromogenic Immunohistochemistry. Two mm slices were immediately removed from the xenograft tumor upon animal sacrifice. The samples were placed in 50 mL of 10% neutral buffered formalin. Tumor slices were kept at room temperature for 7 days before the sample was paraffin embedded, followed by silver staining, Ki67, and F4/80 staining for the visualization of AuNPs, SKOV-3 cancer cells, and dendritic cells and macrophages, respectively. Sample slicing, paraffin embedding, and staining were all performed by University

DOI: 10.1021/acsnano.8b03900
ACS Nano XXXX, XXX, XXX−XXX

Health Network Pathology Research Program Laboratory (UHN-PRP Lab) at University Health Network, Toronto, Canada. The mounted slides of tissue slices were imaged by 3DHistech Pannoramic 250 Flash II slide scanner at SickKids Imaging Facility, Toronto, Canada.

Fluorescent Immunohistochemistry. Five minutes prior to sacrificing the animals, 150 μL of 1 mg/mL of Lectin conjugated with Alexa Fluor 555 was intravenously injected into the animal through tail vein. The conjugation of Lectin to Alexa Fluor 555 was adopted from (4). Upon sacrifice, 2 mm slices were immediately removed from the xenograft tumor and placed in cryomold immersed in OCT solution. The sample was then quickly frozen with liquid nitrogen and kept at −80 °C for storage. For fluorescent staining, Ki67-FITC, F4/80-Cy5, and DAPI were used to visualize the cancer cells, macrophages, and all cells, respectively. The IV injected Lectin-Alexa Fluor 555 was used to visualize blood vessels. After fluorescence imaging of the whole tissue, the coverslips were dismounted from the slide via PBS soaking for 1 h at room temperature, and the sample was stained with Silver kit according to manufacturer's protocol for the visualization of gold nanoparticles. The sample was remounted with Vectashield mounting agent, allowed to solidify overnight, and submitted for imaging the following day. Sample slicing, paraffin embedding, and staining were all performed by University Health Network Pathology Research Program Laboratory (UHN-PRP Lab) at University Health Network, Toronto, Canada. The mounted slides of tissue slices were imaged by 3DHistech Pannoramic 250 Flash II slide scanner at SickKids Imaging Facility, Toronto, Canada.

Perivascular Macrophage Quantification. Smaller fields of view composed of 1 mm^2 in area were randomly cropped from the whole slide scanned images. Image processing was performed in four stages: (1) preprocessing, (2) thresholding, (3) classification, and (4) analysis. In preprocessing, these images were separated into individual fluorescence channels, brightness was normalized across the image, and signal bleed-over was corrected by subtracting the normalized F4/80 channel (labeling macrophages) from the normalized Griffonia Simplificolia Lectin I channel (labeling blood vessels). The images were then automatically thresholded using the Otsu method for nuclei and macrophage channels and the isodata method for blood vessels.[49,50] For the nuclei, the watershed algorithm was used to separate nuclei that were close together and each nuclei was assigned a unique label. Each nuclei was then classified as a macrophage or other cell by dilating the nucleus outline by 10 pixels (9.75 μm) and measuring the proportion of these pixels that were positive for F4/80. If over >20% of pixels within this area was positive for F4/80, the cell was classified as a macrophage.

To isolate cells near the blood vessel, the Griffonia Simplificolia Lectin I (conjugated with Alexa Fluor 555) fluorescence channel was thresholded and expanded for 20 pixels (19.5 μm) radially to include the first cell layer surrounding the blood vessel. Any nuclei that overlaps with the expanded blood vessel region was classified as a perivascular cell. To identify the proportion of macrophages compared to other cells at each distance away from the blood vessel, the blood vessel channel was expanded radially to identify multiple layers of cells. Specifically, we expanded 10 μm to capture the cell proportion between 0 and 10 μm away from blood vessel. We then expanded another 10 μm to capture the cell proportions between 10 and 20 μm and so on.

Note: The MATLAB scripts used for image analysis are in SI, code S1. These scripts require the MATLAB Image Processing Toolbox and the DIPimage toolbox.

Image Analysis of Tumor Histology Slices. Silver stained histology slices counterstained with hematoxylin were manually segmented (hand-traced with stylus via Windows Surface Pro 3) for blood vessels using FIJI. These images were imported into MATLAB and analyzed for nanoparticle permeation using custom scripts (see SI, codes S2–S4). Color deconvolution was performed on the raw image using the method described by Ruifrok *et al.* to extract separate intensity channels for nanoparticles and nuclei.[51] These images were preprocessed to remove faint artifacts and a Gaussian blur was applied to reduce inhomogeneities. Euclidean distance transform applied to the binary imaged of blood vessels was used to determine the distances from each pixel to the nearest blood vessel. We wrote a custom distance histogram function which calculates the mean deconvoluted intensity of nanoparticles at each unit distance from the nearest blood vessels to generate nanoparticle permeation profile. The permeation distance is then defined as the distance from the nearest vessel at which the deconvoluted nanoparticle intensity drops to 50% of its maximum value. The percent of cells accessed is then estimated by taking the percent deconvoluted nuclear stain signal that is located within that distance from blood vessels compared to the total deconvoluted nuclear stain signal.

ASSOCIATED CONTENT

Supporting Information

The Supporting Information is available free of charge on the ACS Publications website at DOI: 10.1021/acsnano.8b03900.

Materials used; gold nanoparticle synthesis; nanoparticle surface modifications; cell culture treatments; animal welfare protocols; biodistribution studies; flow cytometry studies; *in vitro* Matrigel models (PDF)

MATLAB codes (PDF)

AUTHOR INFORMATION

Corresponding Author

*E-mail: warren.chan@utoronto.ca.

ORCID

Stefan Wilhelm: 0000-0003-2167-6221

Warren C. W. Chan: 0000-0001-5435-4785

Author Contributions

Q.D., S.W., D.D., and P.M. performed animal experiments, cell culture, and nanoparticle synthesis. S.W. and Y.Y.C. prepared microchannel setup and toxicity studies. S.S. and Q.D. performed confocal imaging on the microchannel slides. S.S. and Y.Z. performed TEM imaging on nanoparticles and cells. S.W. and P.M. performed ICP data collection. A.M.S. swrote the MATLAB scripts for the histology and microchannel image analysis. Q.D. worked on flow cytometry analysis, histology image analysis, and microchannel image analysis. Q.D., S.W., and W.C.W.C. wrote, edited, and proof-read the manuscript. Q.D., S.W., D.D., S.S., A.M.S., and Y.Y.C. wrote, edited, and organized the supplementary section. W.C.W.C. conceived the original idea.

Notes

The authors declare no competing financial interest.

ACKNOWLEDGMENTS

We acknowledge Natural Sciences and Engineering Research Council of Canada (NSERC), Ontario Graduate Scholarship (OGS), and Canadian Institute of Health Research (CIHR) for financial support. D. Ding thanks financial support from China Scholarship Council. We also acknowledge Dr. Michael Dobosz for his discussions on antibody distribution pattern in the tumor microenvironment. We would like to thank the support of the Canada-Israel Industrial Research and Development Foundation (CIIRDF).

REFERENCES

(1) Sun, T.; Zhang, Y. S.; Pang, B.; Hyun, D. C.; Yang, M.; Xia, Y. Engineered Nanoparticles for Drug Delivery in Cancer Therapy. *Angew. Chem., Int. Ed.* **2014**, *53*, 12320−12364.

(2) Min, Y.; Caster, J. M.; Eblan, M. J.; Wang, A. Z. Clinical Translation of Nanomedicine. *Chem. Rev.* **2015**, *115*, 11147−11190.

DOI: 10.1021/acsnano.8b03900
ACS Nano XXXX, XXX, XXX−XXX

(3) Lammers, T.; Kiessling, F.; Hennink, W. E.; Storm, G. Drug Targeting to Tumors: Principles, Pitfalls and (Pre-) Clinical Progress. *J. Controlled Release* **2012**, *161*, 175−187.
(4) Shi, J.; Kantoff, P. W.; Wooster, R.; Farokhzad, O. C. Cancer Nanomedicine: Progress, Challenges and Opportunities. *Nat. Rev. Cancer* **2017**, *17*, 20−37.
(5) Cheng, J.; Teply, B. A.; Sherifi, I.; Sung, J.; Luther, G.; Gu, F. X.; Levy-Nissenbaum, E.; Radovic-Moreno, A. F.; Langer, R.; Farokhzad, O. C. Formulation of Functionalized PLGA-PEG Nanoparticles for *In Vivo* Targeted Drug Delivery. *Biomaterials* **2007**, *28*, 869−876.
(6) Gref, R.; Lück, M.; Quellec, P.; Marchand, M.; Dellacherie, E.; Harnisch, S.; Blunk, T.; Müller, R. H. 'Stealth' Corona-core Nanoparticles Surface Modified by Polyethylene Glycol (PEG): Influences of the Corona (PEG Chain Length and Surface Density) and of the Core Composition on Phagocytic Uptake and Plasma Protein Adsorption. *Colloids Surf., B* **2000**, *18*, 301−313.
(7) Farokhzad, O. C.; Cheng, J.; Teply, B. A.; Sherifi, I.; Jon, S.; Kantoff, P. W.; Richie, J. P.; Langer, R. Targeted Nanoparticle-Aptamer Bioconjugates for Cancer Chemotherapy. *Proc. Natl. Acad. Sci. U. S. A.* **2006**, *103*, 6315−6320.
(8) Lee, J.-H.; Huh, Y.-M.; Jun, Y.-w.; Seo, J.-w.; Jang, J.-t.; Song, H.-T.; Kim, S.; Cho, E.-J.; Yoon, H.-G.; Suh, J.-S.; Cheon, J. Artificially Engineered Magnetic Nanoparticles for Ultra-Sensitive Molecular Imaging. *Nat. Med.* **2007**, *13*, 95−99.
(9) Tkachenko, A. G.; Xie, H.; Coleman, D.; Glomm, W.; Ryan, J.; Anderson, M. F.; Franzen, S.; Feldheim, D. L. Multifunctional Gold Nanoparticle-Peptide Complexes for Nuclear Targeting. *J. Am. Chem. Soc.* **2003**, *125*, 4700−4701.
(10) Bae, Y. H.; Park, K. Targeted Drug Delivery to Tumors: Myths, Reality and Possibility. *J. Controlled Release* **2011**, *153*, 198−205.
(11) Choi, C. H. J.; Alabi, C. A.; Webster, P.; Davis, M. E. Mechanism of Active Targeting in Solid Tumors with Transferrin-Containing Gold Nanoparticles. *Proc. Natl. Acad. Sci. U. S. A.* **2010**, *107*, 1235−1240.
(12) Kunjachan, S.; Pola, R.; Gremse, F.; Theek, B.; Ehling, J.; Moeckel, D.; Hermanns-Sachweh, B.; Pechar, M.; Ulbrich, K.; Hennink, W. E.; Storm, G.; Lederle, W.; Kiessling, F.; Lammers, T. Passive *Versus* Active Tumor Targeting Using RGD- and NGR-Modified Polymeric Nanomedicines. *Nano Lett.* **2014**, *14*, 972−981.
(13) Kirpotin, D. B.; Drummond, D. C.; Shao, Y.; Shalaby, M. R.; Hong, K.; Nielsen, U. B.; Marks, J. D.; Benz, C. C.; Park, J. W. Antibody Targeting of Long-Circulating Lipidic Nanoparticles Does Not Increase Tumor Localization but Does Increase Internalization in Animal Models. *Cancer Res.* **2006**, *66*, 6732−6740.
(14) Pirollo, K. F.; Chang, E. H. Does a Targeting Ligand Influence Nanoparticle Tumor Localization or Uptake? *Trends Biotechnol.* **2008**, *26*, 552−558.
(15) Wilhelm, S.; Tavares, A. J.; Chan, W. C. W. Reply to "Evaluation of Nanomedicines: Stick to the Basics. *Nat. Rev. Mater.* **2016**, *1*, 16074.
(16) Jain, R. K. Vascular and Interstitial Barriers to Delivery of Therapeutic Agents in Tumors. *Cancer Metastasis Rev.* **1990**, *9*, 253−266.
(17) Wilhelm, S.; Tavares, A. J.; Dai, Q.; Ohta, S.; Audet, J.; Dvorak, H. F.; Chan, W. C. W. Analysis of Nanoparticle Delivery to Tumours. *Nat. Rev. Mater.* **2016**, *1*, 16014.
(18) Jain, R. K.; Stylianopoulos, T. Delivering Nanomedicine to Solid Tumors. *Nat. Rev. Clin. Oncol.* **2010**, *7*, 653−664.
(19) Netti, P. A.; Berk, D. A.; Swartz, M. A.; Grodzinsky, A. J.; Jain, R. K. Role of Extracellular Matrix Assembly in Interstitial Transport in Solid Tumors. *Cancer Res.* **2000**, *60*, 2497−2503.
(20) Lee, H.; Fonge, H.; Hoang, B.; Reilly, R. M.; Allen, C. The Effects of Particle Size and Molecular Targeting on the Intratumoral and Subcellular Distribution of Polymeric Nanoparticles. *Mol. Pharmaceutics* **2010**, *7*, 1195−1208.
(21) Perrault, S. D.; Walkey, C.; Jennings, T.; Fischer, H. C.; Chan, W. C. W. Mediating Tumor Targeting Efficiency of Nanoparticles Through Design. *Nano Lett.* **2009**, *9*, 1909−1915.
(22) Minchinton, A. I.; Tannock, I. F. Drug Penetration in Solid Tumours. *Nat. Rev. Cancer* **2006**, *6*, 583−592.
(23) Chauhan, V. P.; Jain, R. K. Strategies for Advancing Cancer Nanomedicine. *Nat. Mater.* **2013**, *12*, 958−962.
(24) Stylianopoulos, T.; Jain, R. K. Design Considerations for Nanotherapeutics in Oncology. *Nanomedicine* **2015**, *11*, 1893−1907.
(25) Wong, C.; Stylianopoulos, T.; Cui, J.; Martin, J.; Chauhan, V. P.; Jiang, W.; Popovic, Z.; Jain, R. K.; Bawendi, M. G.; Fukumura, D. Multistage Nanoparticle Delivery System for Deep Penetration into Tumor Tissue. *Proc. Natl. Acad. Sci. U. S. A.* **2011**, *108*, 2426−2431.
(26) Anchordoquy, T. J.; Barenholz, Y.; Boraschi, D.; Chorny, M.; Decuzzi, P.; Dobrovolskaia, M. A.; Farhangrazi, Z. S.; Farrell, D.; Gabizon, A.; Ghandehari, H.; Godin, B.; La-Beck, N. M.; Ljubimova, J.; Moghimi, S. M.; Pagliaro, L.; Park, J. H.; Peer, D.; Ruoslahti, E.; Serkova, N. J.; Simberg, D. Mechanisms and Barriers in Cancer Nanomedicine: Addressing Challenges, Looking for Solutions. *ACS Nano* **2017**, *11*, 12−18.
(27) Miller, M. A.; Zheng, Y.-R.; Gadde, S.; Pfirschke, C.; Zope, H.; Engblom, C.; Kohler, R. H.; Iwamoto, Y.; Yang, K. S.; Askevold, B.; Kolishetti, N.; Pittet, M.; Lippard, S. J.; Farokhzad, O. C.; Weissleder, R. Tumour-Associated Macrophages Act as a Slow-Release Reservoir of Nano-Therapeutic Pt(IV) Pro-drug. *Nat. Commun.* **2015**, *6*, 8692.
(28) Miao, L.; Newby, J. M.; Lin, C. M.; Zhang, L.; Xu, F.; Kim, W. Y.; Forest, M. G.; Lai, S. K.; Milowsky, M. I.; Wobker, S. E.; Huang, L. The Binding Site Barrier Elicited by Tumor-Associated Fibroblasts Interferes Disposition of Nanoparticles in Stroma-Vessel Type Tumors. *ACS Nano* **2016**, *10*, 9243−9258.
(29) Baxter, L. T.; Jain, R. K. Transport of Fluid and Macromolecules in Tumors. I. Role of Interstitial Pressure and Convection. *Microvasc. Res.* **1989**, *37*, 77−104.
(30) Wiig, H.; Swartz, M. A. Interstitial Fluid and Lymph Formation and Transport: Physiological Regulation and Roles in Inflammation and Cancer. *Physiol. Rev.* **2012**, *92*, 1005−1060.
(31) Jiang, W.; Kim, B. Y. S.; Rutka, J. T.; Chan, W. C. W. Nanoparticle-Mediated Cellular Response is Size-Dependent. *Nat. Nanotechnol.* **2008**, *3*, 145−150.
(32) Colombo, M.; Fiandra, L.; Alessio, G.; Mazzucchelli, S.; Nebuloni, M.; De Palma, C.; Kantner, K.; Pelaz, B.; Rotem, R.; Corsi, F.; Parak, W. J.; Prosperi, D. Tumour Homing and Therapeutic Effect of Colloidal Nanoparticles Depend on the Number of Attached Antibodies. *Nat. Commun.* **2016**, *7*, 13818.
(33) Scott, A. M.; Wolchok, J. D.; Old, L. J. Antibody Therapy of Cancer. *Nat. Rev. Cancer* **2012**, *12*, 278−287.
(34) Sykes, E. A.; Dai, Q.; Sarsons, C. D.; Chen, J.; Rocheleau, J. V.; Hwang, D. M.; Zheng, G.; Cramb, D. T.; Rinker, K. D.; Chan, W. C. W. Tailoring Nanoparticle Designs to Target Cancer Based on Tumor Pathophysiology. *Proc. Natl. Acad. Sci. U. S. A.* **2016**, *113*, E1142−51.
(35) Hauck, T. S.; Ghazani, A. A.; Chan, W. C. W. Assessing the Effect of Surface Chemistry on Gold Nanorod Uptake, Toxicity, and Gene Expression in Mammalian Cells. *Small* **2008**, *4*, 153−159.
(36) Chattopadhyay, N.; Cai, Z.; Pignol, J.-P.; Keller, B.; Lechtman, E.; Bendayan, R.; Reilly, R. M. Design and Characterization of Her-2-Targeted Gold Nanoparticles for Enhanced X-Radiation Treatment of Locally Advanced Breast Cancer. Mol. *Mol. Pharmaceutics* **2010**, *7*, 2194−2206.
(37) Dai, Q.; Walkey, C.; Chan, W. C. W. Polyethylene Glycol Backfilling Mitigates the Negative Impact of the Protein Corona on Nanoparticle Cell Targeting. *Angew. Chem., Int. Ed.* **2014**, *53*, 5093−5096.
(38) Chithrani, B. D.; Ghazani, A. A.; Chan, W. C. W. Determining the Size and Shape Dependence of Gold Nanoparticle Uptake into Mammalian Cells. *Nano Lett.* **2006**, *6*, 662−668.
(39) Lu, F.; Wu, S.-H.; Hung, Y.; Mou, C.-Y. Size Effect on Cell Uptake in Well-Suspended, Uniform Mesoporous Silica Nanoparticles. *Small* **2009**, *5*, 1408−1413.
(40) Tang, L.; Yang, X.; Yin, Q.; Cai, K.; Wang, H.; Chaudhury, I.; Yao, C.; Zhou, Q.; Kwon, M.; Hartman, J. A.; Dobrucki, I. T.; Dobrucki, L. W.; Borst, L. B.; Lezmi, S.; Helferich, W. G.; Ferguson, A. L.; Fan, T. M.; Cheng, J. Investigating the Optimal Size of

DOI: 10.1021/acsnano.8b03900
ACS Nano XXXX, XXX, XXX−XXX

Anticancer Nanomedicine. *Proc. Natl. Acad. Sci. U. S. A.* **2014**, *111*, 15344−15349.
(41) Sykes, E. A.; Chen, J.; Zheng, G.; Chan, W. C. W. Investigating the Impact of Nanoparticle Size on Active and Passive Tumor Targeting Efficiency. *ACS Nano* **2014**, *8*, 5696−5706.
(42) Miller, M. A.; Gadde, S.; Pfirschke, C.; Engblom, C.; Sprachman, M. M.; Kohler, R. H.; Yang, K. S.; Laughney, A. M.; Wojtkiewicz, G.; Kamaly, N.; Bhonagiri, S.; Pittet, M. J.; Farokhzad, O. C.; Weissleder, R. Predicting Therapeutic Nanomedicine Efficacy Using a Companion Magnetic Resonance Imaging Nanoparticle. *Sci. Transl. Med.* **2015**, *7*, 314ra183.
(43) Tsvetkova, Y.; Beztsinna, N.; Baues, M.; Klein, D.; Rix, A.; Golombek, S. K.; Al Rawashdeh, W.; Gremse, F.; Barz, M.; Koynov, K.; Banala, S.; Lederle, W.; Lammers, T.; Kiessling, F. Balancing Passive and Active Targeting to Different Tumor Compartments Using Riboflavin-Functionalized Polymeric Nanocarriers. *Nano Lett.* **2017**, *17*, 4665−4674.
(44) Mazzucchelli, S.; Bellini, M.; Fiandra, L.; Truffi, M.; Rizzuto, M. A.; Sorrentino, L.; Longhi, E.; Nebuloni, M.; Prosperi, D.; Corsi, F. Nanometronomic Treatment of 4T1 Breast Cancer with Nanocaged Doxorubicin Prevents Drug Resistance and Circumvents Cardiotoxicity. *Oncotarget* **2017**, *8*, 8383−8396.
(45) Fritz, J. M.; Tennis, M. A.; Orlicky, D. J.; Lin, H.; Ju, C.; Redente, E. F.; Choo, K. S.; Staab, T. A.; Bouchard, R. J.; Merrick, D. T.; Malkinson, A. M.; Dwyer-Nield, L. D. Depletion of Tumor-Associated Macrophages Slows the Growth of Chemically Induced Mouse Lung Adenocarcinomas. *Front. Immunol.* **2014**, *5*, 587.
(46) Zeisberger, S. M.; Odermatt, B.; Marty, C.; Zehnder-Fjällman, A. H. M.; Ballmer-Hofer, K.; Schwendener, R. A. Clodronate-Liposome-Mediated Depletion of Tumour-Associated Macrophages: A New and Highly Effective Antiangiogenic Therapy Approach. *Br. J. Cancer* **2006**, *95*, 272−281.
(47) Pradel, L. P.; Ooi, C.-H.; Romagnoli, S.; Cannarile, M. A.; Sade, H.; Rüttinger, D.; Ries, C. H. Macrophage Susceptibility to Emactuzumab (RG7155). *Mol. Cancer Ther.* **2016**, *15*, 3077−3086.
(48) Vangara, K. K.; Liu, J. L.; Palakurthi, S. Hyaluronic Acid-Decorated PLGA-PEG Nanoparticles for Targeted Delivery of SN-38 to Ovarian Cancer. *Anticancer Res.* **2013**, *33*, 2425−2434.
(49) Ridler, T. W.; Calvard, S. Picture Thresholding Using an Iterative Selection Method. *IEEE Trans. Syst., Man, Cybern.* **1978**, *8*, 630−632.
(50) Otsu, N. A Threshold Selection Method from Gray-Level Histograms. *IEEE Trans. Syst., Man, Cybern.* **1979**, *9*, 62−66.
(51) Ruifrok, A. C.; Johnston, D. A. Quantification of Histochemical Staining by Color Deconvolution. *Anal. Quant. Cytol. Histol.* **2001**, *23*, 291−299.

DOI: 10.1021/acsnano.8b03900
ACS Nano XXXX, XXX, XXX−XXX